Revealing Atomic Structure and Oxidation States of Dopants in Charge-Ordered Nanoparticles for Migration-Promoted Oxygen Exchange Capacity

Xiangbin Cai[1], Kaiyun Chen[2], Xiang Gao[3], Chao Xu[4], Mingzi Sun[5], Guanyu Liu[3], Xuyun Guo[4], Yuan Cai[1], Bolong Huang[5], Junkai Deng[2], Jefferson Zhe Liu[7], Antonio Tricoli[3], Ning Wang[1], Christian Dwyer[6], Ye Zhu[4]*

[1]*Department of Physics and Center for Quantum Materials, The Hong Kong University of Science and Technology, Clear Water Bay, Kowloon, Hong Kong, China*

[2]*State Key Laboratory for Mechanical Behavior of Materials, Xi'an Jiaotong University, 710049, China*

[3]*Nanotechnology Research Laboratory, Research School of Engineering, Australian National University, Canberra, ACT 2601, Australia*

[4]*Department of Applied Physics, The Hong Kong Polytechnic University, Hung Hom, Kowloon, Hong Kong, China*

[5]*Department of Applied Biology and Chemical Technology, The Hong Kong Polytechnic University, Hung Hom, Kowloon, Hong Kong, China*

[6]*Department of Physics, Arizona State University, Tempe, Arizona 85287, USA*

[7]*Department of Mechanical Engineering, The University of Melbourne, Parkville, Victoria, Australia*

**yezhu@polyu.edu.hk*

ABSTRACT

Doping of nanomaterials has become a versatile approach to tailor their physical and chemical properties, leading to the emerging fields of solotronics and quantum-controlled catalysis. These extraordinary functionalities critically depend on the atomic arrangements and dynamic behaviors of dopants, which are however challenging to probe due to the ultrasmall volume of hosting nanomaterials and the even smaller scale of doping-induced structure variations. Here we reveal the characteristic configurations of Ce dopants and their correlation with the remarkably enhanced oxygen-exchange capacity in < 10 nm Mn_3O_4 nanoparticles. The element and oxidation-state sensitivity, and quantification capability of atomic-resolution electron energy-loss spectroscopic mapping allow an unambiguous determination of substitutional solitary Ce dopants and CeO_2 nanoclusters inside the charge-ordered Mn_3O_4 matrix, as well as single-atomic-layer CeO_x on the surface. The observed high mobility of Ce dopants further

illustrates an effective pathway for the conversion between various dopant nanophases. Our observation provides atomic-scale evidence of the oxygen-exchange mechanism through dopant migration in Ce-doped Mn_3O_4 nanoparticles, which rationalizes their superior redox efficiency and oxygen-exchange capacity for thermochemical synthesis of solar fuels. The demonstrated characterization strategy capable of directly probing local atomic and electronic structures of dopants is widely applicable to the investigation of structure-property interplay in other doping-engineered nanomaterials.

INTRODUCTION

Structural engineering of nanocrystals via doping offers an additional degree of freedom to tune their functionalities and boost their performance.[1-8] As for chemically reactive nanoparticles, both the redox behaviors controlled by the electronic structure and the reactive centers on surface can be significantly improved by doping, even with a low-concentration of foreign atoms. For example, Mo doping in Pt_3Ni nanoparticles can lead to exceptional oxygen reduction reaction performance with activity ~4 times better than the pure Pt_3Ni and ~80 times better than the commercial Pt catalyst.[9] Understanding the effects of doping requires knowledge not only about the overall doping parameters, such as dopant concentration and uniformity, but also on the exact atomic configurations of dopants[10-11], including the preferential sites, bonding and ordering, and their dynamic behaviors[12-13] in the host lattice. Such knowledge will in turn contribute to the rational nanomaterial design and process optimization,[14-16] ideally at the atomic scale. On the other hand, the extremely small dimension of nanoparticles and the even smaller scale of the dopant structure make it a formidable task to determine the atomic and electronic structures of dopants. Conventional diffraction and spectroscopy methods can only yield average sample information, which are insensitive to the local short-range structural fluctuations caused by doping.[17] Annular dark field (ADF) imaging in scanning transmission electron microscopy (STEM) has served as a powerful tool to directly probe dopants in real space, which can identify the position of a single dopant atom[18-21] and the atomic structure of dopant clusters[10, 22-23]. However, ADF imaging is only effective when the doping species are of heavier elements compared to the hosting materials, and is incapable of obtaining any electronic-structure information.

Electron energy-loss spectroscopy (EELS) in STEM is a promising technique complementing the normal ADF imaging.[24] The characteristic energy-loss signals offer elemental sensitivity down to the atomic scale, which do not suffer the limitation of heavy doping elements.[25-26] Furthermore, the fine structures of energy-loss edges carry valuable electronic-structure information, making EELS a unique approach to probe local chemical bonding and oxidation states atomic-column by atomic-column.[27-31] On the other hand, unlike normal ADF imaging which primarily uses the elastically scattered electrons with a large scattering cross section, energy-loss signals from intrinsically weak inelastic scattering require much longer acquisition time and higher sample stability to achieve sufficient signal-to-noise ratio. Nanoparticles in size of only several nanometers are much less mechanically stable (unless embedded in a matrix[32]) and thus challenging for atomic-resolution EELS mapping. In particular, despite of few pioneering works using EELS to detect dopants and doping clusters in nanoparticles,[33-34] the potential of atomic-scale EELS quantification and oxidation-state mapping on dopants in nanoparticles has not been investigated.

Here we demonstrate quantitative dopant-atom counting and oxidation-state mapping using atomic-resolution EELS on an important nanoparticle system, Ce-doped Mn_3O_4 nanoparticles < 10 nm in size. As reaction agents for the thermochemical redox synthesis of solar fuels, the 3 at% Ce-doped Mn_3O_4 nanoparticles < 10 nm in size have been demonstrated to possess substantially enhanced redox efficiency and oxygen-exchange capacity than that of the pure Mn_3O_4 as well as benchmark CeO_2 nanoparticles, offering 8 times higher CO yields than CeO_2.[35] Ce doping enables an efficient redox cycle between manganese oxides and carbide, which cannot be achieved in pure Mn_3O_4 and thus is responsible for such a remarkable performance enhancement.[35] However, the exact behavior of Ce dopants remains unknown, with only the hypothesis that Ce doping promoted oxygen mobility that further facilitates the oxide-carbide conversion.[35-36] In this work, we utilize the robust element and oxidation-state sensitivity of atomic-resolution EELS mapping, as well as quantification capability down to the single-dopant limit, to reveal the characteristic structure and oxidation states of Ce dopants both inside the Mn_3O_4 lattice and on the surface. These experimental results are further rationalized by density functional theory (DFT) calculations and enable us to propose an atomic-scale oxygen exchange mechanism which

explains the doping-enhanced redox efficiency and oxygen-exchange capacity in Ce-doped Mn_3O_4 nanoparticles.

RESULTS AND DISCUSSION

Imaging Solitary Ce inside Charge-Ordered Mn_3O_4 Matrix

Ultrafine Mn_3O_4 nanoparticles doped with 3 at% Ce were synthesized through one-step flame spray pyrolysis. **Fig. 1a** shows an atomic-resolution ADF image of the Ce-doped Mn_3O_4 nanoparticle in size of ~9 nm. The image exhibits single-crystal Mn_3O_4 lattice up to the surface without any disordered layer, showing high crystal quality. The Ce dopants can be roughly identified from the higher image intensity in some atomic columns as the line profile shows (^{58}Ce is heavier than ^{25}Mn). Although such a projection image cannot directly tell whether the observed Ce dopants are embedded inside the Mn_3O_4 lattice or absorbed at the surface sites, the achieved high spatial resolution (0.87 Å) allows the detection of subtle lattice expansion (4.2%) caused by Ce incorporated inside Mn_3O_4 (**Fig. S1**). X-ray photoelectron spectroscopy (XPS) further indicates the primary existence of Ce is indeed inside Mn_3O_4 nanoparticles (**Fig. S2**). Powder X-ray diffraction, Raman spectroscopy and electron diffraction (**Fig. S3**) all confirm that doping Ce does not introduce any phase changes into the pristine Mn_3O_4 hausmannite phase, consistent with the atomic-resolution images.

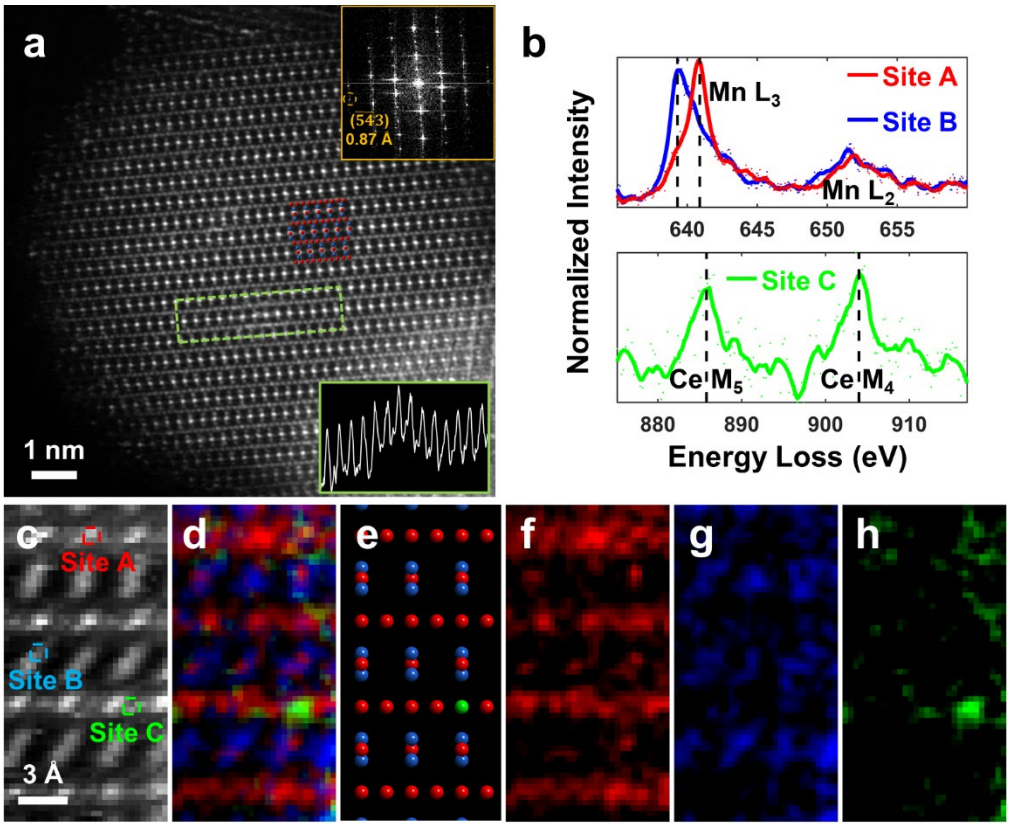

Fig. 1: Single dopant sensitivity of EELS in the charge-ordered Mn_3O_4 nanoparticle. a, *Atomic-resolution ADF image of a typical Ce-doped Mn_3O_4 nanoparticle at <101> zone axis with the atomic model overlaid and an extracted line profile inset at the bottom-right corner. The Fourier transform of imaged lattice at the top-right corner indicates the high spatial resolution (0.87 Å) achieved.* ***b,*** *Averaged EEL spectra of the Mn $L_{2,3}$ and Ce $M_{4,5}$ edges of marked sites in the simultaneous ADF image* ***c****. The Mn L_3 edge shows 1.6 eV chemical shift for different Mn oxidation states, i.e. Mn^{3+} L_3 at 641.2 eV and Mn^{2+} L_3 at 639.6 eV. The Ce $M_{4,5}$ edges are clearly above the noise level and match Ce^{4+}. Atomic-resolution EELS mapping* ***d*** *of a solitary Ce dopant embedded inside the charge-ordered Mn_3O_4 matrix, with color-coded components of Mn^{3+}* ***f****, Mn^{2+}* ***g****, Ce^{4+}* ***h****. The corresponding atomic model, where red, blue and green balls represent Mn^{3+}, Mn^{2+} and Ce^{4+}, respectively, is presented in* ***e****. The challenge of atomic-resolution EELS mapping on ultrafine nanoparticles is reflected by the noticeable noise and distortions, which are due to the inevitable particle drift and instability during the long-time data acquisition.*

Unlike ADF imaging, EELS provides a more reliable approach with single-dopant sensitivity. As illustrated in **Fig. 1c and 1d**, atomic-resolution EELS enables us to pinpoint the position of a solitary Ce dopant atom. It is noteworthy that the Ce atom does not show discernable contrast in the ADF image. The ADF image in **Fig. 1c** derives from electrons which are scattered to high angles as the electron beam scans over the various atomic columns. A single Ce dopant in a 9-nm-thick Mn^{3+} column, as we have in **Fig. 1c** (estimated using the EELS low-loss signal[37]), may cause little change in the high-angle scattering compared to a pure Mn^{3+} column, leading to the 'invisible' dopant in the ADF image. While ADF is typically sensitive to heavy dopant atoms such as Ce, the lack of contrast in the present case is attributable to the competing scattering effects when the depth of the Ce dopant is greater than 6 nm at the Mn_3O_4 <101> zone axis (**Fig. S4**). EELS mapping, on the other hand, can give binary contrast for atomic columns, with and without dopants, in an element-selective manner. EELS is also less sensitive to the dopant depth, as indicated by our simulation (**Fig. S4**), which makes it more reliable than ADF imaging for mapping the Ce dopants. We note that similar conclusion was drawn by Gunawan *et al.* using Mn dopants inside ZnSe nanocrystals,[33] but only based on non-atomic-resolution EELS mapping and simplified calculations. Also, in contrast to their system of light Mn dopants in the heavy ZnSe matrix, our work here demonstrates that even for heavy dopants like Ce, EELS is still more sensitive and reliable than ADF imaging. More examples of Ce dopant detection using EELS mapping are presented in the following figures as well as in **Fig. S7**. Negligible beam effects (such as knock-on damage or structure modification) are identified after EELS mapping, with one example and the electron irradiation test demonstrated in **Fig. S10**. Moreover, our beam propagation simulation as shown in **Fig. S11** demonstrates that for the thickness range and major zone axes of our nanoparticles, the electron beam will be mostly confined in one Mn column with only minor spreading and no cross-talk from the neighboring Mn columns, confirming the determined dopant-atom positions to be reliable.

EELS fine-structure analysis further allows us to distinguish the ordered arrangements of Mn^{3+} and Mn^{2+} cations in Mn_3O_4, and therefore to determine the preferential substitution sites of Ce dopants. The step-by-step data processing is shown in **Fig. S5**, which demonstrates the capability of oxidation-state mapping using the chemical shift of Mn $L_{2,3}$ edges to reveal the charge ordering

in ultrafine Mn_3O_4 nanoparticles.[30] Comparing the Ce map (**Fig. 1h**) with the Mn^{3+} and Mn^{2+} maps (**Figs. 1f and 1g**), it is clear that the Ce dopant preferentially substitutes Mn^{3+} in this charge-ordered system. It is reasonable given that the larger space in oxygen octahedra and the higher anion coordination number of Mn^{3+} sites, compared to those of the tetrahedral Mn^{2+} sites, lead to more energetically favorable occupation of Ce^{4+} (1.63 eV lower in energy according to our DFT calculations). The preference of Ce dopants to occupy Mn^{3+} sites is consolidated by EELS mapping of Ce nanoclusters and adsorbates presented below.

Uncovering CeO_2 Nanoclusters by Dopant-Atom Counting

Atomic-resolution EELS also enables quantitative dopant-atom counting in each Mn^{3+} column. Due to multiple scattering of the electron beam, both the ADF and EELS intensity varies as a function of dopant depth even for the same amount of dopant.[38-39] It thus invalidates the strict linear proportionality between the EELS intensity and the amount of dopant. However, our EELS simulation indicates that under our experimental conditions, the Ce $M_{4,5}$ edge intensity only varies slightly as a function of dopant depth, much smaller than the intensity change due to dopant numbers. For example, EELS intensity from a single dopant at various depth appears to be a flat line compared to the intensity from multiple dopants, as shown in **Fig. 2c**. Such a small depth effect is attributed to small sample thickness of the ultrafine nanoparticles (6 nm) as well as the large EELS collection angle (91 mrad), which minimizes the multiple scattering effect. With the weak dependence on dopant depth, the Ce EELS intensity exhibits an approximately linear correlation with the amount of dopant atoms (**Fig. 2c**), which can be utilized for dopant-atom counting. Although the intensity spread indicated by the error bars becomes larger for more Ce dopant atoms, the error bars from the neighboring data points do not overlap which guarantees the capability of dopant quantification. With the clear integer relationship in the integrated Ce EELS intensities from different doped columns, as shown in **Fig. 2d**, we can derive the amount of dopant atoms in each column and propose a three-dimensional atomic structure of the dopant cluster as shown in **Fig. 2e**. It matches closely to a CeO_2 unit cell aligned along its <110> zone axis, representing a commensurate intercalating CeO_2 nanocluster inside Mn_3O_4 lattice with CeO_2 <110> || Mn_3O_4 <021> and CeO_2 {002} || Mn_3O_4 {200}. With all the Ce dopants taking the place

of Mn^{3+}, the nearest Ce-Ce distance is ~5.769 Å which is close to the lattice parameter of CeO_2 (5.415 Å). It is therefore expected to be a relatively low-energy configuration, which explains the high frequency of this coherent type of cluster with another example shown in **Fig. S6**.

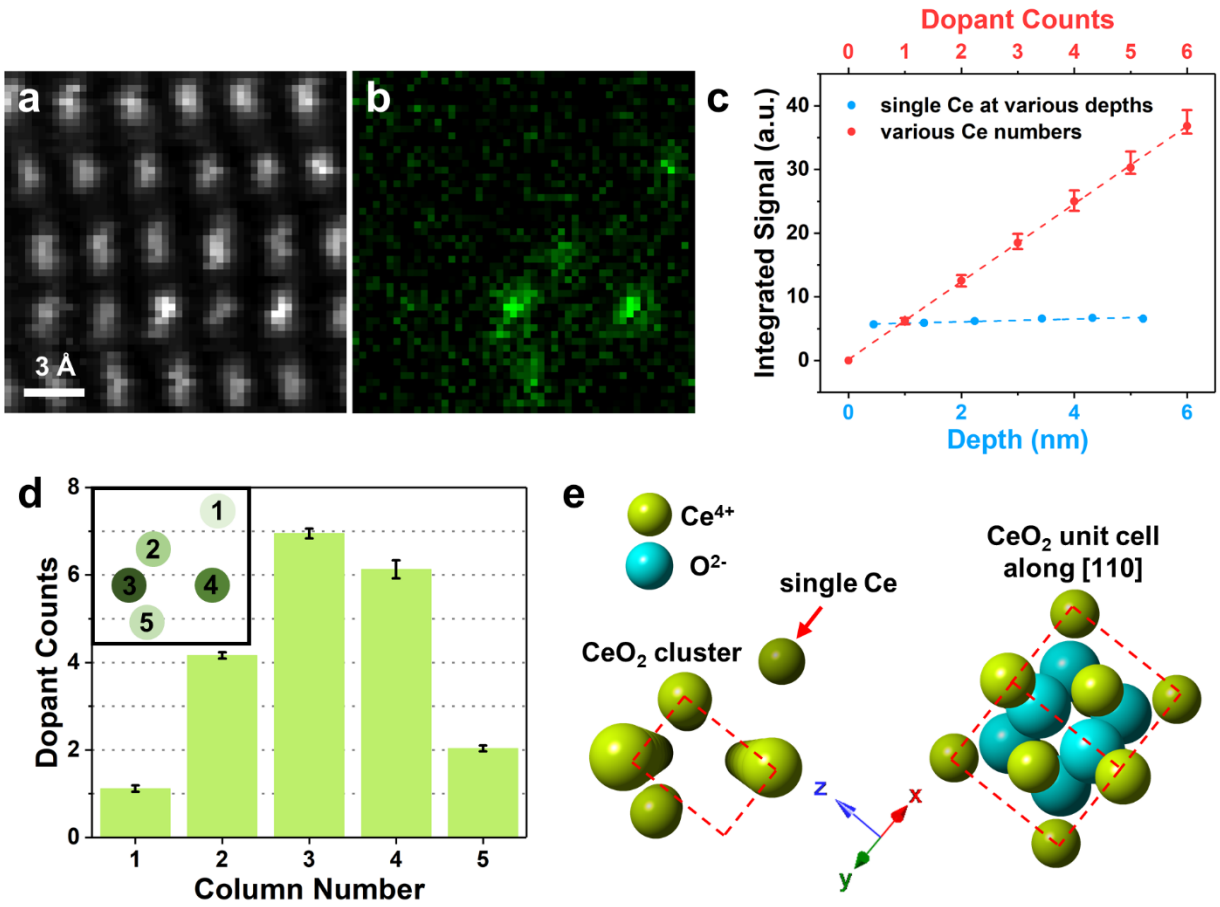

Fig. 2: Three-dimensional atomic structure of an embedded CeO_2 nanocluster. a, *Simultaneous ADF image showing the Mn_3O_4 lattice along <021> zone axis.* ***b,*** *EELS map integrated from the Ce $M_{4,5}$ edges.* ***c,*** *EELS simulation using experimental conditions for a single Ce located at various column depths and different numbers of Ce at various depths in a fixed column. The red dots represent the average intensity, and the intensity spread indicated by the error bar is due to Ce dopants at different depths.* ***d,*** *Dopant-atom counting from the Ce $M_{4,5}$ map* ***b*** *by integrating the intensity of each atomic column and comparing with the simulation.* ***e,*** *Three-dimensional atomic structure of the Ce nanocluster deduced from the quantitative dopant-atom counting (left panel), well consistent with the CeO_2 structure oriented along [110] zone axis (right panel).*

CeO_x Adsorbates and Oxidation States of Dopant Structure

Besides embedded Ce dopants, surface Ce has also been discovered to form single-atomic-layer Ce adsorbates at the {101} facets of Mn_3O_4 nanoparticles, as shown in **Fig. 3a** and more in **Fig. S8**. The atomic-resolution EELS map in **Fig. 3d** clearly reveals that the Ce dopants only substitute surface Mn^{3+} sites, consistent with the behaviors of Ce dopants inside Mn_3O_4 lattice. But different from those embedded Ce dopants, Ce adsorbates on {101} facets show lower oxidation states as indicated by the fine structures of Ce $M_{4,5}$ edges (**Fig. 3b**). Both the chemical shift towards lower energy and the slightly higher M_5/M_4 ratio compared to the embedded Ce dopants (0.79 versus 0.68) indicate that Ce^{4+} is partially reduced to Ce^{3+} at the Mn_3O_4 surface.[40-41] We note that the single-atomic-layer adsorbates are stable under the electron beam, as demonstrated in **Fig. S10 c&d**, indicating that Ce^{3+} is not created by the reduction effect of the electron beam. Under the assumption that all the surface Mn^{3+} sites are occupied by Ce, a proposed structure model is presented in **Fig. S8c**, which may represent a meta-stable CeO_x (x = 1.5 - 2) phase on the surface of Mn_3O_4. According to the statistics on all our TEM images, around 70% imaged {101} facets are covered by such single-atomic-layer CeO_x adsorbates. This selective distribution of atomically thin CeO_x adsorbates with matched hexagonal lattice at the {101} facets of Mn_3O_4 nanoparticles may help to lower the total surface energy and also produce anisotropic redox activity of different crystal facets in Ce-doped Mn_3O_4 nanoparticles.[42-44]

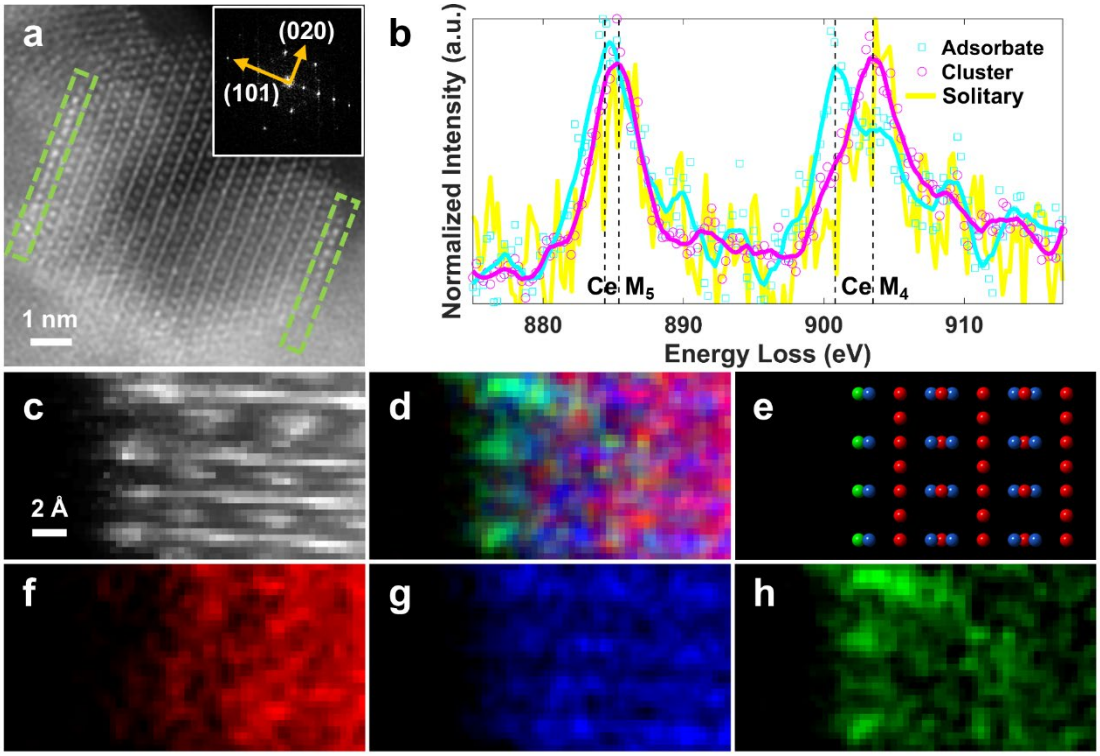

Fig. 3: Surface CeO_x adsorbates and their oxidation states. a, *Atomic-resolution ADF image showing the typical single-atomic-layer CeO_x adsorbates formed at the {101} facets of a Mn_3O_4 nanoparticle. The FFT of the nanoparticle lattice is inset at the top-right corner.* ***b,*** *Averaged EEL spectra of Ce $M_{4,5}$ edges from various Ce nanophases, i.e. a solitary Ce in* ***Fig. 1****, a CeO_2 cluster in* ***Fig. 2*** *and the adsorbate, carefully aligned to the absolute energy-loss scale using simultaneously recorded zero-loss peaks. The Ce M_5 and Ce M_4 edge onsets of the adsorbate shift towards lower energy-loss by 1.0 eV and 2.7 eV, respectively, indicating a lower oxidation state.* ***d,*** *Atomic-resolution EELS mapping on the CeO_x adsorbate with the simultaneous ADF image* ***c****, deduced atomic model* ***e*** *and color-coded components of Mn^{3+}* ***f****, Mn^{2+}* ***g****, $Ce^{4/3+}$* ***h****.*

In contrast to embedded Ce dopants which may modify the physical (such as bandgap) and chemical properties (such as oxygen mobility) of Mn_3O_4, dopants sitting at the nanoparticle surface can have a more direct impact on the redox activity. Facets of CeO_2 have been reported as active sites for catalytic reactions, whose activity largely depends on the formation of oxygen vacancies.[6, 45] The single-atomic-layer CeO_x at Mn_3O_4 {101} surfaces can be considered a special form of CeO_2 facets containing oxygen vacancies, the presence of which is indicated by the reduced oxidation state of Ce in **Fig. 3b** and verified by our DFT calculations: within the hexagonal lattice of surface Ce dopant, oxygen atoms at the center of the sublayer Ce triangles can easily displace by 2 Å spontaneously and produce vacancies at the original sites, as indicated by the oxygen migration path and corresponding energy diagram in **Fig. S9**. It indicates excellent oxygen-release capability which is essential in strengthening the adsorption of CH_4 in the combustion reaction or other redox reaction intermediates.[6, 45] The following C-H dissociation can be further facilitated by the surface oxygen vacancies and the Ce reducibility.[46] Therefore, our observation and calculations demonstrate the possible mechanism of surface oxygen being activated by the nearby Ce dopants, which can assist the transportation of other species and enhance the redox reactions such as the oxidation of CH_4.

Oxygen-Exchange Mechanism by Dopant Structure Evolution

We further observe high mobility of Ce dopants inside Mn_3O_4 lattice, which suggests an effective oxygen-exchange route in addition to the above mechanism. Sequential atomic-resolution ADF images of a Ce-doped Mn_3O_4 nanoparticle are shown in **Fig. 4b and 4c**, in which the Ce dopant substitutions can be distinguished from the line profiles. The octahedral sites of Mn^{3+} are again demonstrated to be more stable substitution positions for Ce^{4+}. More strikingly, the identified dopant can hop freely between the octahedral Mn^{3+} sites. We then applied DFT calculations of the energy barriers to elucidate the detailed migration paths. The migration paths were calculated by assuming that there are Mn^{3+} vacancies next to Ce^{4+} to balance the local charge and facilitate its migration,[47] rather than a direct Mn^{3+}-Ce^{4+} ion exchange that is less favorable. Other effects of Ce migration on the surrounding Mn_3O_4 lattice were not considered in our calculation.

As shown in **Fig. 4d**, every Mn^{3+} site (Oct1) has three types of neighboring octahedral Mn^{3+} sites: one along <111> directions (Oct2), one long <010> directions (Oct3) and the last along <100> (Oct4). With a Ce sitting at Oct1, our calculation indicates that the migration of Ce from Oct1 to Oct2 can be accomplished by passing through an open space within an oxygen octahedron, while the easiest path for Ce migration from Oct1 to Oct3 is through an oxygen tetrahedron. The larger inner space of oxygen octahedra than that of oxygen tetrahedra results in a two-fold lower energy barrier (0.43 eV). Although Ce could also migrate to Oct4 by passing through an oxygen octahedron, the Mn^{2+} chains on the halfway drastically increase the migration barrier. We therefore conclude that Ce migration tends to occur between neighboring octahedral Mn^{3+} sites along <111> directions in Mn_3O_4.

The above observation suggests that various nanophases of Ce dopants can be converted to one another through the identified Ce migration: considering the observed Ce nanophases are in an equilibrium state, adding reductive agents such as methane may significantly favor the migration of solitary Ce^{4+} onto surface to form the reactive single-layer CeO_x adsorbate and bring out lattice oxygen for reaction.[36] The capability of mobile Ce^{4+} to carry oxygen or create oxygen vacancies to enhance oxygen transport has been reported in many other systems,[48-49] and is also evidenced by the reduced Mn oxidation states caused by Ce doping as shown in **Fig. S2**. The resulting decrease of solitary Ce^{4+} concentration in Mn_3O_4 lattice may further cause the dissolution of CeO_2 nanoclusters into solitary Ce^{4+} as mobile oxygen carriers, which continues until all Ce^{4+} is used up. The opposite process will occur under an oxidative environment, in which Ce can bring more oxygen in to achieve more complete oxidation. This is consistent with the reported Ce exsolution during Mn_3O_4 reduction and reincorporation of Ce during the oxidation reactions to form manganese oxides.[35] Such an oxygen-exchange process promoted by Ce-dopant migration may dramatically enhance the oxygen mobility in the Ce-doped Mn_3O_4 nanoparticles, enabling a complete reduction from Mn_3O_4 to Mn_7C_3 with superior oxygen-exchange capacity as well as redox efficiency. In contrast, without Ce doping, pure Mn_3O_4 can only be partially reduced primarily to the MnO phase under the same reaction condition.[35] Given that the small fraction of Ce dopant will not change thermodynamics of Mn_3O_4 reduction, the difference must be oxygen mobility and the associated redox kinetics that are boosted by Ce migration, which explains the

exceptional performance of Ce-doped Mn_3O_4 nanoparticles in thermochemical synthesis of solar fuels. It is worth noting that despite the magnificent role of Ce dopants, too much Ce doping (≥5%) will lead to larger scale CeO_2 second phases that do not dissolve as easily as the nanocluster, and thus mitigate the performance enhancement.

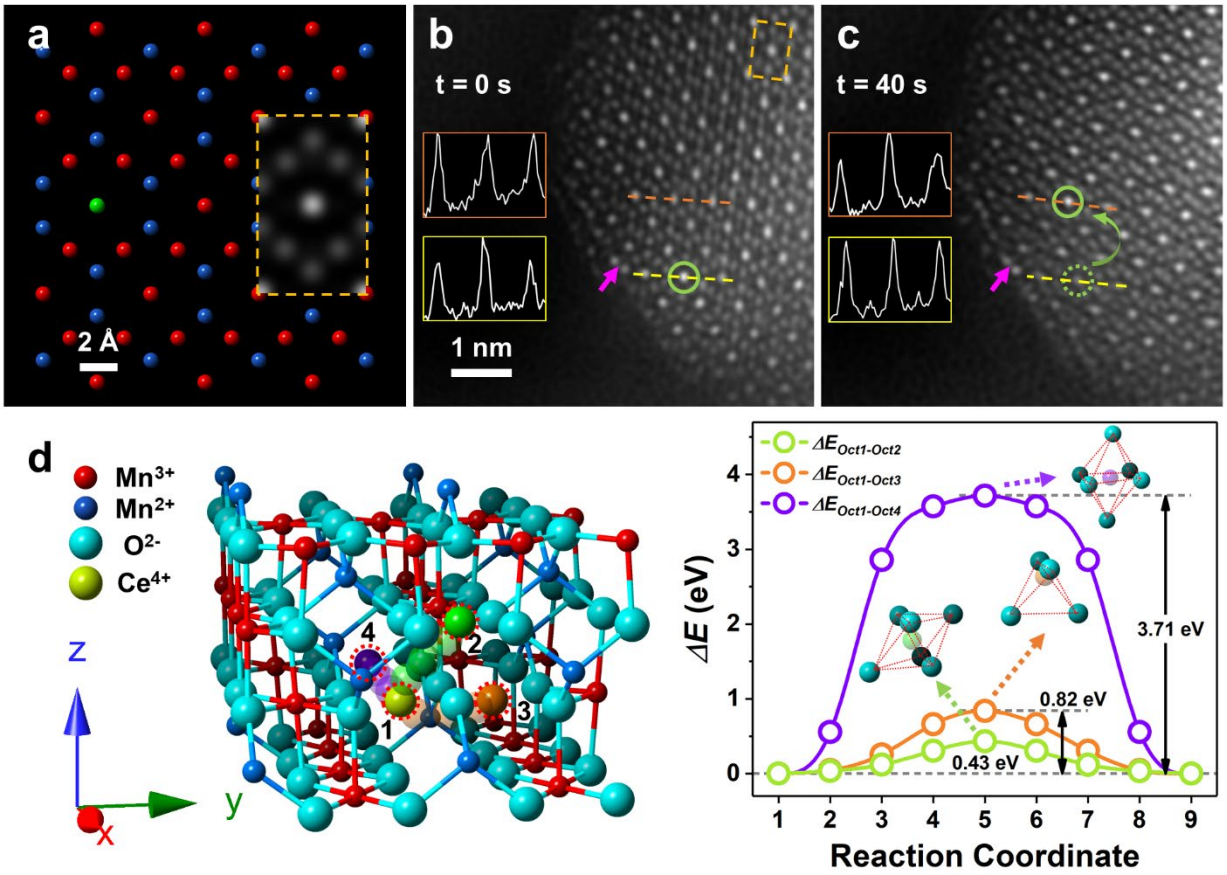

Fig. 4: Low-barrier dopant migration. a, *Atomic structure viewed along the <100> zone axis of Mn_3O_4 overlaid with the simulated ADF image of a Mn_3O_4 unit cell. The green ball indicates a typical Mn^{3+} column containing Ce^{4+}.* ***b, c,*** *Sequential atomic-resolution ADF images demonstrating the fast dopant migration between Mn^{3+} sites. The line profiles across the dopant-occupied columns are inset on the left. Magenta arrows serve as the position mark to guide the eyes.* ***d,*** *Three possible migration paths (towards site 2, 3, 4) for a substitutional Ce are illustrated in the left panel, where semi-transparent balls represent the intermediate transit steps of the Ce in correspondence to the data points in the energy plot in the right panel. The total energy change as a function of reaction coordinate (transit steps) in the right panel are calculated by assuming that there is a neighboring Mn vacancy to balance the local charge. The insets are the atomic models of intermediate Ce-O-coordinated structures corresponding to respective energy barriers.*

Conclusion

In summary, we demonstrate the element and oxidation-state sensitivity of EELS mapping down to the single-dopant limit using the ultrafine 3 at% Ce-doped Mn_3O_4 nanoparticles (< 10 nm), which outperforms conventional ADF-STEM imaging. Various dopant structures and oxidation states are confidently revealed at the atomic scale, including the substitutional solitary Ce^{4+}, CeO_2 nanoclusters embedded inside Mn_3O_4 matrix and single-atomic-layer CeO_x adsorbate at the {101} facets of Mn_3O_4 surface. These Ce phases are believed to be correlated by the observed high dopant mobility for an effective oxygen-exchange route, which provides an atomic-scale understanding of the enhanced redox efficiency and oxygen-exchange capacity by Ce doping. At last, the EELS mapping demonstrated in this work offers a powerful tool to explore dopant structure and behaviors at the atomic scale, and to deliver critical insights for better understanding and subsequent design of structure-property interplay in doping-engineered nanomaterials.

METHODS

Sample Synthesis: The ultrafine pure Mn_3O_4 and 3 at% Ce-doped Mn_3O_4 nanoparticles were synthesized using a custom-built flame spray pyrolysis setup. The precursor liquid solution for synthesizing pure Mn_3O_4 was prepared by dissolving manganese (III) acetylacetonate (Sigma Aldrich, technical grade) in 2-ethylhexanoic acid (Sigma Aldrich, purity ≥ 99%) with a total atomic concentration of Mn ions at 0.4 mol·L^{-1}. Similarly, the precursor solution for synthesizing 3 at% Ce-doped Mn_3O_4 was prepared by mixing cerium (III) acetate hydrate (Sigma Aldrich, purity 99.9%) with manganese acetylacetonate at a Ce/Mn atomic ratio of 3:97 and dissolving the mixture in 2-ethylhexanoic acid with an atomic concentration of total metal ions at 0.4 mol·L^{-1}. Both solutions were heated in 368 K oil bath and subsequently added with equal volumetric amount of xylene to reach a total metal ion concentration of 0.2 mol·L^{-1}. The final combustible solutions were fed at 5 mL·min^{-1} rate through a nozzle and atomized with an oxygen flow of 5 SLPM (grade 4.0) with a pressure drop of ca. 4 bar. The resulted spray was ignited with a surrounding annular premixed methane (flow rate of 1.2 SLPM, grade 4.5) and oxygen (flow rate of 2 SLPM, grade 4.0) flame. Nanoparticle powders were collected with a vacuum pump (ICME Type M80B4) on water-cooled glass-fiber filters (Sartorius glass microfiber, 150 mm diameter) placed at ca. 40 cm height above the burner.

STEM Characterization: Both pure and Ce-doped nanoparticle samples were dispersed and sonicated in high-purity ethanol. Then solution was dropped onto 400-mesh lacey-carbon copper grid for natural drying. STEM imaging and spectroscopy were performed using JEOL JEM ARM 200CF equipped with a cold field emission gun and an ASCOR fifth-order probe corrector. ADF imaging and STEM-EELS experiments were carried out under 200 kV accelerating voltage with a 26 mrad convergence semi angle for the optimal information transfer. To achieve minimized beam damage, we conducted the EELS mapping with the least necessary electron dose by reducing the probe current (from over 100 to 24 pA), pixel numbers (0.03 nm/pixel) and dwell time (10 ms/pixel) for such nanoparticles. The depth of focus is around 7 nm, near the typical Ce-doped Mn_3O_4 nanoparticle size. The collection semi angles for ADF signal were set to 68-200 mrad. In STEM-EELS experiments, energy dispersion of 0.25 eV per channel was selected and 91 mrad collection semi angle of Gatan Enfinium ER spectrometer was set up. Zero-loss peak and core-loss edges were simultaneously recorded in dual EELS mode. The simultaneous ADF signal was acquired with a 93 mrad inner collection semi angle.

ADF Simulation: Multislice codes by Earl J. Kirkland[50] is used for the atomic-resolution ADF image simulation to handle the dynamical scattering process of transmitted electrons. An aberration-free electron probe is assumed using experimental parameters. The probe is then focused and scanned on the crystal surface. The Ce adatom is modelled as one Ce substituting the Mn^{3+} ion in the first atomic layer while the Ce dopant is modelled as one Ce substituting a Mn^{3+} ion in different depths. Four phonon configurations were included to represent the thermal-diffuse scattering effect at room temperature (20 phonon configurations were also tested but no obvious difference was seen because of the ultra-thin sample thickness), and the effective source size was considered by convolving simulated images with a 2D Gaussian function of 0.6 Å FWHM. The Debye Waller factors used for Mn and O ions are those in hausmannite phase, i.e. 0.2 $Å^2$ and

0.32 $Å^2$, respectively. The Debye Waller factor for Ce cations is assumed to be the same as that in CeO_2 compound, i.e. 0.5 $Å^2$.

EELS Simulation: EELS is simulated using a multislice code including multiple-elastic, multiple-thermal-diffuse, and single-core-loss scattering. Inelastic core-loss scattering is calculated using atomic wave functions computed with the Cowan code[51]. Elastic and thermal-diffuse scattering both before and after the inelastic scattering event has been considered (so called 'double channeling approximation').[52-53] The thermal diffuse scattering was included using the frozen-phonon algorithm, with thermal parameters taken from the literature, and averaged over eight atomic configurations. The simulations employed supercells ~3 nm in size for all crystal structures, sampled using 1,024 × 1,024 pixels for the STEM-ADF calculations (to ensure accuracy in the high-angle scattering) and 512 × 512 pixels for the core-loss calculations.

DFT Calculations: The Vienna Ab-inito Simulation Package (VASP)[54] was used to conduct the DFT calculations by the projector-augmented wave method. The spin-polarized generalized gradient approximation (GGA) with the Perdew-Burke-Ernzerhof (PBE) functional was adopted here.[55-56] The kinetic energy cutoff for wavefunction expansion was set to 520 eV. Monkhorst-Pack k-point grid[57] of 5x5x5 was used for 1x1x1 unit cell and similar density of k-point grid was used for 2x2x1 supercell to ensure the k-point sampling spacing is smaller than 0.1 $Å^{-1}$, respectively. Atomic positions and lattice constants were fully relaxed until the difference of energy and forces were less than 10^{-5} eV and 0.01 eV/Å. The nudged elastic band (NEB) method[58] was employed to study the possible migration paths of Ce dopant from one to another Mn^{3+} octahedral sites in 2x2x1 supercell. During the NEB calculation, the shape and volume of supercell were fixed.

ACKNOWLEDGEMENT

Y. Z. thanks the financial support from the Research Grants Council of Hong Kong through the Early Career Scheme (Project No. 25301617) and the Hong Kong Polytechnic University grant (Project No. 1-ZE6G). N. W. thanks the financial support from the Research Grants Council of Hong Kong (Project Nos. C6021-14E and 16306818). J. Z. L. acknowledges supports from Australian Research Council through Discovery Project (DP180101744) and from high performance computing facility from National Computational Infrastructure of Australia. J. D. acknowledges the financial support from National Science Foundation of China (Grant number: 51728203, 51471126). A. T. thanks the financial support from the ARC Discovery Project (#150101939) and the ARC Discovery Early Career Award (#160100569). B. H. thanks the support from the Natural Science Foundation of China (NSFC) for the Youth Scientist grant (Grant No.: NSFC 11504309, 21771156) and the Early Career Scheme (ECS) fund from the Research Grants Council of Hong Kong (Grant No.: PolyU 253026/16P).

AUTHOR CONTRIBUTIONS

Y. Z. led the project. X. G., G. L. and A. T. synthesized the nanoparticles. X. C. performed the STEM characterization and ADF simulations. C. D. conducted the EELS simulations. K. C., J. D. and J. Z. L. carried out the DFT calculations for embedded Ce dopants. M. S. and B. H. designed the model and did DFT calculations for surface Ce dopants. X. C. and Y. Z. analyzed the characterization data

and wrote the paper. All authors participated in the discussion of results and commented on the manuscript.

ADDITIONAL INFORMATION

Supporting information (including **Fig. S1-11**) is available in a separate file. The authors declare no competing financial interests. Correspondence and requests for materials should be addressed to Y. Z. (yezhu@polyu.edu.hk).

REFERENCE

1. Norris, D. J.; Efros, A. L.; Erwin, S. C., Doped nanocrystals. *Science* **2008,** *319* (5871), 1776-1779.
2. Beaulac, R.; Schneider, L.; Archer, P. I.; Bacher, G.; Gamelin, D. R., Light-induced spontaneous magnetization in doped colloidal quantum dots. *Science* **2009,** *325* (5943), 973-976.
3. Bussian, D. A.; Crooker, S. A.; Yin, M.; Brynda, M.; Efros, A. L.; Klimov, V. I., Tunable magnetic exchange interactions in manganese-doped inverted core-shell ZnSe-CdSe nanocrystals. *Nature materials* **2009,** *8* (1), 35-40.
4. Koenraad, P. M.; Flatté, M. E., Single dopants in semiconductors. *Nature materials* **2011,** *10* (2), 91-100.
5. Mocatta, D.; Cohen, G.; Schattner, J.; Millo, O.; Rabani, E.; Banin, U., Heavily doped semiconductor nanocrystal quantum dots. *Science* **2011,** *332* (6025), 77-81.
6. Ke, J.; Xiao, J.-W.; Zhu, W.; Liu, H.; Si, R.; Zhang, Y.-W.; Yan, C.-H., Dopant-induced modification of active site structure and surface bonding mode for high-performance nanocatalysts: CO oxidation on capping-free (110)-oriented CeO_2: Ln (Ln= La–Lu) nanowires. *Journal of the American Chemical Society* **2013,** *135* (40), 15191-15200.
7. Buonsanti, R.; Milliron, D. J., Chemistry of doped colloidal nanocrystals. *Chemistry of Materials* **2013,** *25* (8), 1305-1317.
8. Guo, D.; Shibuya, R.; Akiba, C.; Saji, S.; Kondo, T.; Nakamura, J., Active sites of nitrogen-doped carbon materials for oxygen reduction reaction clarified using model catalysts. *Science* **2016,** *351* (6271), 361-365.
9. Huang, X.; Zhao, Z.; Cao, L.; Chen, Y.; Zhu, E.; Lin, Z.; Li, M.; Yan, A.; Zettl, A.; Wang, Y. M., High-performance transition metal–doped Pt_3Ni octahedra for oxygen reduction reaction. *Science* **2015,** *348* (6240), 1230-1234.
10. Voyles, P.; Muller, D.; Grazul, J.; Citrin, P.; Gossmann, H.-J., Atomic-scale imaging of individual dopant atoms and clusters in highly n-type bulk Si. *Nature* **2002,** *416* (6883), 826-829.
11. Zhang, S.; Katz, M. B.; Dai, S.; Zhang, K.; Du, X.; Graham, G. W.; Pan, X., New Atomic-Scale Insight into Self-Regeneration of Pt-$CaTiO_3$ Catalysts: Incipient Redox-Induced Structures Revealed by a Small-Angle Tilting STEM Technique. *The Journal of Physical Chemistry C* **2017,** *121* (32), 17348-17353.
12. Yan, P.; Zheng, J.; Zhang, J.-G.; Wang, C., Atomic resolution structural and chemical imaging revealing the sequential migration of Ni, Co, and Mn upon the battery cycling of layered cathode. *Nano letters* **2017,** *17* (6), 3946-3951.
13. Gent, W. E.; Lim, K.; Liang, Y.; Li, Q.; Barnes, T.; Ahn, S.-J.; Stone, K. H.; McIntire, M.; Hong, J.; Song, J. H., Coupling between oxygen redox and cation migration explains unusual electrochemistry in lithium-rich layered oxides. *Nature communications* **2017,** *8* (1), 2091.
14. Wu, Q.; Yan, B.; Cen, J.; Timoshenko, J.; Zakharov, D. N.; Chen, X.; Xin, H. L.; Yao, S.; Parise, J. B.; Frenkel, A. I., Growth of Nanoparticles with Desired Catalytic Functions by Controlled Doping-Segregation of Metal in Oxide. *Chemistry of Materials* **2018,** *30* (5), 1585-1592.

15. Hofman, E.; Robinson, R. J.; Li, Z.-J.; Dzikovski, B.; Zheng, W., Controlled dopant migration in CdS/ZnS core/shell quantum dots. *Journal of the American Chemical Society* **2017,** *139* (26), 8878-8885.
16. Lee, W.; Oh, J.; Kwon, W.; Lee, S. H.; Kim, D.; Kim, S., Synthesis of Ag/Mn Co-Doped CdS/ZnS (Core/Shell) Nanocrystals with Controlled Dopant Concentration and Spatial Distribution, and Dynamics of Excitons and of Energy Transfer between Co-Dopants. *Nano Letters* **2019**, 19, 308-317.
17. Billinge, S. J.; Levin, I., The problem with determining atomic structure at the nanoscale. *Science* **2007,** *316* (5824), 561-565.
18. Shibata, N.; Findlay, S.; Azuma, S.; Mizoguchi, T.; Yamamoto, T.; Ikuhara, Y., Atomic-scale imaging of individual dopant atoms in a buried interface. *Nature materials* **2009,** *8* (8), 654-658.
19. Krivanek, O. L.; Chisholm, M. F.; Nicolosi, V.; Pennycook, T. J.; Corbin, G. J.; Dellby, N.; Murfitt, M. F.; Own, C. S.; Szilagyi, Z. S.; Oxley, M. P., Atom-by-atom structural and chemical analysis by annular dark-field electron microscopy. *Nature* **2010,** *464* (7288), 571-574.
20. Bar-Sadan, M.; Barthel, J.; Shtrikman, H.; Houben, L., Direct imaging of single Au atoms within GaAs nanowires. *Nano letters* **2012,** *12* (5), 2352-2356.
21. Hwang, J.; Zhang, J. Y.; D'Alfonso, A. J.; Allen, L. J.; Stemmer, S., Three-dimensional imaging of individual dopant atoms in $SrTiO_3$. *Physical review letters* **2013,** *111* (26), 266101.
22. Couillard, M.; Radtke, G.; Knights, A. P.; Botton, G. A., Three-dimensional atomic structure of metastable nanoclusters in doped semiconductors. *Physical review letters* **2011,** *107* (18), 186104.
23. Lacroix, B.; Genevois, C.; Doualan, J.; Brasse, G.; Braud, A.; Ruterana, P.; Camy, P.; Talbot, E.; Moncorgé, R.; Margerie, J., Direct imaging of rare-earth ion clusters in Yb: CaF_2. *Physical Review B* **2014,** *90* (12), 125124.
24. Batson, P., Simultaneous STEM imaging and electron energy-loss spectroscopy with atomic-column sensitivity. *Nature* **1993,** *366* (6457), 727-728.
25. Kimoto, K.; Asaka, T.; Nagai, T.; Saito, M.; Matsui, Y.; Ishizuka, K., Element-selective imaging of atomic columns in a crystal using STEM and EELS. *Nature* **2007,** *450* (7170), 702-704.
26. Suenaga, K.; Sato, Y.; Liu, Z.; Kataura, H.; Okazaki, T.; Kimoto, K.; Sawada, H.; Sasaki, T.; Omoto, K.; Tomita, T., Visualizing and identifying single atoms using electron energy-loss spectroscopy with low accelerating voltage. *Nature chemistry* **2009,** *1* (5), 415-418.
27. Bosman, M.; Keast, V.; Garcia-Munoz, J.; D'alfonso, A.; Findlay, S.; Allen, L., Two-dimensional mapping of chemical information at atomic resolution. *Physical Review Letters* **2007,** *99* (8), 086102.
28. Muller, D.; Kourkoutis, L. F.; Murfitt, M.; Song, J.; Hwang, H.; Silcox, J.; Dellby, N.; Krivanek, O., Atomic-scale chemical imaging of composition and bonding by aberration-corrected microscopy. *Science* **2008,** *319* (5866), 1073-1076.
29. Lazar, S.; Shao, Y.; Gunawan, L.; Nechache, R.; Pignolet, A.; Botton, G. A., Imaging, core-loss, and low-loss electron-energy-loss spectroscopy mapping in aberration-corrected STEM. *Microscopy and Microanalysis* **2010,** *16* (4), 416-424.

30. Tan, H.; Turner, S.; Yücelen, E.; Verbeeck, J.; Van Tendeloo, G., 2D atomic mapping of oxidation states in transition metal oxides by scanning transmission electron microscopy and electron energy-loss spectroscopy. *Physical review letters* **2011,** *107* (10), 107602.
31. Gloter, A.; Badjeck, V.; Bocher, L.; Brun, N.; March, K.; Marinova, M.; Tencé, M.; Walls, M.; Zobelli, A.; Stéphan, O., Atomically resolved mapping of EELS fine structures. *Materials Science in Semiconductor Processing* **2017,** *65*, 2-17.
32. Torruella, P.; Ruiz-Caridad, A.; Walls, M.; Roca, A. G.; López-Ortega, A.; Blanco-Portals, J.; López-Conesa, L.; Nogués, J.; Peiró, F.; Estradé, S., Atomic-Scale Determination of Cation Inversion in Spinel-Based Oxide Nanoparticles. *Nano letters* **2018,** *18* (9), 5854-5861.
33. Gunawan, A. A.; Mkhoyan, K. A.; Wills, A. W.; Thomas, M. G.; Norris, D. J., Imaging "invisible" dopant atoms in semiconductor nanocrystals. *Nano letters* **2011,** *11* (12), 5553-5557.
34. Rossell, M. D.; Ramasse, Q. M.; Findlay, S. D.; Rechberger, F.; Erni, R.; Niederberger, M., Direct imaging of dopant clustering in metal-oxide nanoparticles. *ACS nano* **2012,** *6* (8), 7077-7083.
35. Gao, X.; Liu, G.; Zhu, Y.; Kreider, P.; Bayon, A.; Gengenbach, T.; Lu, T.; Liu, Y.; Hinkley, J.; Lipiński, W., Earth-abundant transition metal oxides with extraordinary reversible oxygen exchange capacity for efficient thermochemical synthesis of solar fuels. *Nano Energy* **2018,** *50*, 347-358.
36. Imamura, S.; Shono, M.; Okamoto, N.; Hamada, A.; Ishida, S., Effect of cerium on the mobility of oxygen on manganese oxides. *Applied Catalysis A: General* **1996,** *142* (2), 279-288.
37. Egerton, R. F., *Electron energy-loss spectroscopy in the electron microscope*. Springer Science & Business Media: 2011.
38. Zhu, Y.; Soukiassian, A.; Schlom, D.; Muller, D.; Dwyer, C., Towards artifact-free atomic-resolution elemental mapping with electron energy-loss spectroscopy. *Applied Physics Letters* **2013,** *103* (14), 141908.
39. Tan, H.; Zhu, Y.; Dwyer, C.; Xin, H. L., Energy-loss-and thickness-dependent contrast in atomic-scale electron energy-loss spectroscopy. *Physical Review B* **2014,** *90* (21), 214305.
40. Garvie, L.; Buseck, P., Determination of Ce^{4+}/Ce^{3+} in electron-beam-damaged CeO_2 by electron energy-loss spectroscopy. *Journal of Physics and Chemistry of solids* **1999,** *60* (12), 1943-1947.
41. Song, K.; Schmid, H.; Srot, V.; Gilardi, E.; Gregori, G.; Du, K.; Maier, J.; van Aken, P. A., Cerium reduction at the interface between ceria and yttria-stabilised zirconia and implications for interfacial oxygen non-stoichiometry. *APL Materials* **2014,** *2* (3), 032104.
42. Hettiarachchi, M.; Abdelhamid, E.; Nadgorny, B.; Brock, S. L., Anisotropic Manganese Antimonide Nanoparticle Formation by Solution-Solid-Solid Growth Mechanism: Consequence of Sodium Borohydride Addition Towards Reduced Surface Oxidation and Enhanced Magnetic Moment. *Nanoscale* **2019**, 11, 6886-6896.
43. Shi, R.; Wang, J.; Cai, X.; Zhang, L.; Chen, P.; Liu, S.; Zhang, L.; Ouyang, W.; Wang, N.; Cheng, C., Axial Modulation of Metal-Insulator Phase Transition of VO_2 Nanowires by Graded Doping Engineering for Optically Readable Thermometers. *The Journal of Physical Chemistry C* **2017,** *121* (44), 24877-24885.

44. Shi, R.; Cai, X.; Wang, W.; Wang, J.; Kong, D.; Cai, N.; Chen, P.; He, P.; Wu, Z.; Amini, A., Single-Crystalline Vanadium Dioxide Actuators. *Advanced Functional Materials* **2019**, 29, 1900527.
45. Tian, D.; Li, K.; Wei, Y.; Zhu, X.; Zeng, C.; Cheng, X.; Zheng, Y.; Wang, H., DFT insights into oxygen vacancy formation and CH_4 activation over CeO_2 surfaces modified by transition metals (Fe, Co and Ni). *Physical Chemistry Chemical Physics* **2018,** *20* (17), 11912-11929.
46. Zhu, T.; Kundakovic, L.; Dreher, A.; Flytzani-Stephanopoulos, M., Redox chemistry over CeO_2-based catalysts: SO_2 reduction by CO or CH_4. *Catalysis Today* **1999,** *50* (2), 381-397.
47. Mizoguchi, T.; Takahashi, N.; Lee, H.-S., First-principles study on migration mechanism in $SrTiO_3$. *Applied Physics Letters* **2011,** *98* (9), 091909.
48. Trovarelli, A., Catalytic properties of ceria and CeO_2-containing materials. *Catalysis Reviews* **1996,** *38* (4), 439-520.
49. Skorodumova, N.; Simak, S.; Lundqvist, B. I.; Abrikosov, I.; Johansson, B., Quantum origin of the oxygen storage capability of ceria. *Physical Review Letters* **2002,** *89* (16), 166601.
50. Kirkland, E. J., *Advanced computing in electron microscopy*. Springer Science & Business Media: 2010.
51. Cowan, R. D., *The theory of atomic structure and spectra*. Univ of California Press: 1981.
52. Dwyer, C., Multislice theory of fast electron scattering incorporating atomic inner-shell ionization. *Ultramicroscopy* **2005,** *104* (2), 141-151.
53. Dwyer, C.; Findlay, S.; Allen, L., Multiple elastic scattering of core-loss electrons in atomic resolution imaging. *Physical Review B* **2008,** *77* (18), 184107.
54. Kresse, G.; Furthmüller, J., Efficiency of ab-initio total energy calculations for metals and semiconductors using a plane-wave basis set. *Computational materials science* **1996,** *6* (1), 15-50.
55. Perdew, J. P.; Chevary, J. A.; Vosko, S. H.; Jackson, K. A.; Pederson, M. R.; Singh, D. J.; Fiolhais, C., Atoms, molecules, solids, and surfaces: Applications of the generalized gradient approximation for exchange and correlation. *Physical Review B* **1992,** *46* (11), 6671.
56. Blöchl, P. E., Projector augmented-wave method. *Physical review B* **1994,** *50* (24), 17953.
57. Monkhorst, H. J.; Pack, J. D., Special points for Brillouin-zone integrations. *Physical review B* **1976,** *13* (12), 5188.
58. Henkelman, G.; Uberuaga, B. P.; Jónsson, H., A climbing image nudged elastic band method for finding saddle points and minimum energy paths. *The Journal of chemical physics* **2000,** *113* (22), 9901-9904.

TABLE OF CONTENTS GRAPHIC